ACS Partner Journal

CHEM & BIO ENGINEERING

pubs.acs.org/ChemBioEng

Article

Insight into the Role of Hydroxypropyl Cellulose in Tuning Crystallization Behaviors of DL-Methionine

Hong Yin, Sen Xia, Zhirong Chen, and Shenfeng Yuan*

Cite This: *Chem Bio Eng.* 2024, 1, 704–714

Read Online

ACCESS | Metrics & More | Article Recommendations | Supporting Information

ABSTRACT: Efficient regulation of DL-methionine (DL-met) crystallization behavior remains of great interest since it usually appears in the form of needles or flakes, which is prone to cause problems in downstream processes. In this study, the crystallization process and crystal morphology of DL-met were focused with hydroxypropyl cellulose (HPC) as the tuning additive. The crystallization behaviors of DL-met with HPC were investigated through experiments and theoretical calculations from thermodynamic and kinetic perspectives to understand the mechanism of HPC in the DL-met crystal morphology. It was found that HPC could raise the interfacial energy γ, making nucleation more difficult. Furthermore, the inhibitory effect of HPC on the axial direction growth was much stronger than that on the radial direction, thereby changing the DL-met crystal morphology from rod-like to block-like. Theoretical calculations explained the underlying mechanism of HPC in regulating crystal habits. Due to the structural differences between different crystal surfaces, HPC exhibited a stronger hydrogen bonding with the (111) crystal surface, thus notably hindering its growth, specifically in the axial direction.

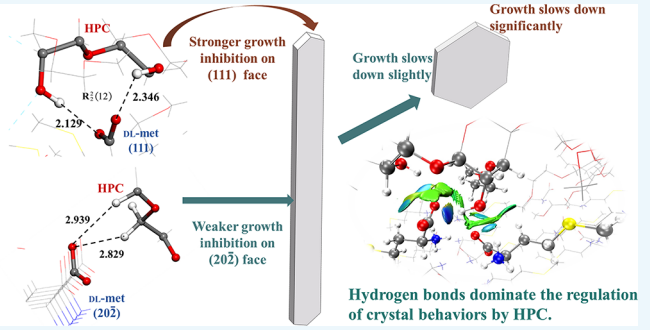

KEYWORDS: *DL-methionine, hydroxypropyl cellulose, crystallization behavior, crystal morphology, theoretical computation, hydrogen bond*

1. INTRODUCTION

DL-methionine (DL-met) is one of the "backbone" amino acids for protein synthesis in living organisms, which is essential for physiological balance and health, and is widely used in medicine, food, feed, and cosmetics.[1,2] Qualified DL-met products are separated and purified by crystallization, and their crystal morphology and size are critical for downstream processes. Flaky and needle-like crystals are prone to agglomeration and breakage, which results in poor flowability and low bulk density, thus affecting subsequent processes such as mixing, slurrying, and tablet pressing, while bulk crystals are easier to filter or mix and are preferred in industrial processes.[3,4] Currently, DL-met products obtained by crystallization mostly appear as needles or sheets, which makes the industrial crystallization process high in energy consumption and low in product quality. Therefore, it is crucial to investigate the modification and regulation of the DL-met crystal behavior.

Generally, the crystal morphology depends on the relative growth rates of different crystal surfaces. The faster the growth in a given direction, the lower the morphological importance.[5,6] It has been found that process conditions, such as cooling rate and stirring rate, have very limited abilities to engineer the crystal morphology.[7−11] In particular, some crystals have strong hydrogen bonds in their internal structure, leading to the overgrowth of specific crystal surfaces, thus making the formation of needle habits.[12] Unfortunately, the process conditions have a much weaker ability to modify the crystal habits of strongly hydrogen-bonded systems. In contrast, the effect of additives on the regulation of crystal behavior is remarkable and highly efficient. For instance, Yin et al.[13] obtained the β form of DL-met with a small aspect ratio by using inorganic acids or bases during the cooling and evaporation crystallization. Molecular dynamics simulations showed that met^+ and met^- could not only occupy the "kink sites" on the crystal surface but also destroy the solvation layer, thus making changes in crystal habits. Li et al.[14] selected DL-leucine as a tailor-made additive for hindering the nucleation and growth of the β form of DL-met and successfully obtained the α form. However, studies related to the effect of polymeric additives on the crystallization behavior of DL-met have rarely reported. Cellulose derivatives, such as carboxymethylcellulose (CMC) and hydroxypropyl cellulose (HPC), are utilized in

Received: September 8, 2023
Revised: December 25, 2023
Accepted: December 25, 2023
Published: January 9, 2024

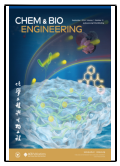

https://doi.org/10.1021/cbe.3c00024
Chem Bio Eng. 2024, 1, 704–714

many fields such as food, packaging, and biomedicine due to their biocompatible and biodegradable properties.[15−18] To be specific, CMC is mainly used in biomedical research in the form of hydrogels for tissue engineering, wound healing, and drug delivery.[19,20] As an edible, cost-effective and versatile cellulose derivative, HPC is used in pharmaceutical and food industries,[21,22] which has little application in the design of regulating crystallization processes. Its molecular structure, as shown in Figure 1(a), contains a large number of hydroxyl

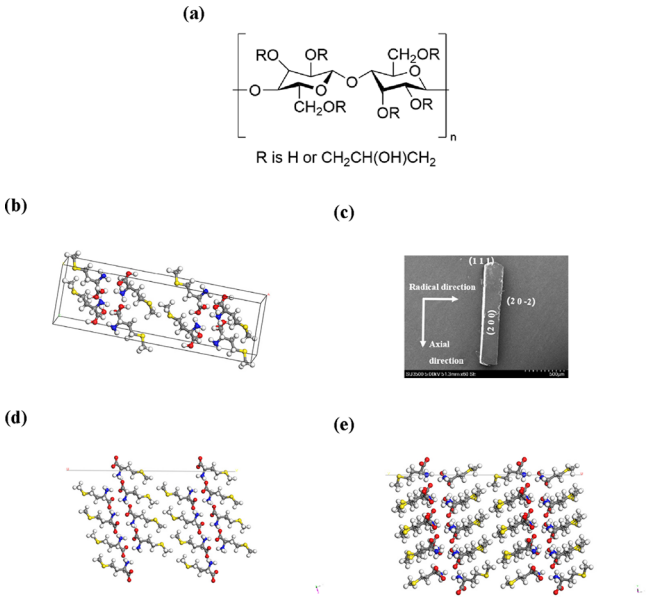

Figure 1. (a) HPC molecule structure, (b) unit cell structure of the β form DL-met, (c) crystal morphology and crystal surface index of DL-met, (d) $(20\bar{2})$ crystal surface, and (e) (111) crystal surface.

groups, which are expected to interact with the ammonium and carboxylate on the DL-met molecule in solution to change the growth rate of different crystal surfaces in different degrees, thus further modifying the crystal habits.

Nucleation behavior is the first step in the crystallization process and plays a decisive role in determining crystal morphology.[23−27] According to the classical nucleation theory (CNT), the expression for the primary homogeneous nucleation rate (J) is as follows[28]

$$J = A\ \exp\left(-\frac{\Delta G_c}{kT}\right) \tag{1}$$

where A is the pre-exponential factor, ΔG_c is the critical nucleation free energy, k is the Boltzmann constant, and T is the solution temperature. In supersaturated solutions, solute molecules combine with each other to form crystal embryos, which need to overcome a certain nucleation energy barrier to form nuclei. The expression of the nucleation free energy $\Delta G(r)$ of the embryo is as follows[29]

$$\Delta G(r) = -\left(\frac{k_v r^3}{v}\right)kT\ \ln(S) + k_a r^2\gamma \tag{2}$$

where k_v and k_a are the volume and area shape factors, and when the particles are spherical, their values are $4\pi/3$ and 4π, respectively. $S = C/C^*$, wherein S, C, and C^* are the supersaturation ratio, the concentration of the solution, and the saturated solution concentration, respectively; γ is the interfacial energy between the crystal and the solution and usually determines the crystal growth mechanism. As the number of solute molecules in the crystal embryo increases, $\Delta G(r)$ first increases and then decreases, and its maximum value is the critical nucleation free energy ΔG_c. At this point, the corresponding size of the crystal embryo is the critical nucleus particle size r_{crit}. Crystals with a particle size smaller than r_{crit} automatically dissolve and disappear, while those larger than r_{crit} continue to grow until they become nuclei.

By taking the derivative of eq 2 and applying $\frac{\partial \Delta G(r)}{\partial r} = 0$, the critical nucleation nucleus r_{crit}, critical nucleation free energy ΔG_c, and critical molecular number i_{crit} for primary homogeneous nucleation can be obtained:

$$r_{crit} = \frac{2k_a u\gamma}{3k_v kT\ \ln(S)} = \frac{2u\gamma}{kT\ \ln(S)} \tag{3}$$

$$\Delta G_c = \frac{k_a (r_{crit})^2\gamma}{3} = \frac{16\pi\gamma^3 v^2}{3(kT\ \ln(S))^2} \tag{4}$$

$$i = \frac{4\pi (r_{crit})^3}{3v} \tag{5}$$

Substituting eq 1 into eq 4,

$$J = A\ \exp\left(-\frac{16\pi\gamma^3 v^2}{3k^3T^3\ \ln(S)}\right) \tag{6}$$

According to the mononuclear model proposed by Kashchiev,[30] the induction time is assumed to be inversely proportional to the rate of primary nucleation in the homogeneous nucleation process.

$$t_{ind} \propto \frac{1}{J} \tag{7}$$

Substituting eq 7 with eq 6 gives the nucleation induction time and supersaturation as a function of the following,

$$\ln t_{ind} = B + \frac{16\pi\gamma^3 v^2}{3k^3T^3\ \ln^2(S)} \tag{8}$$

K is the slope of the plot of $\ln t_{ind}$ against $1/\ln^2 S$ and B is a constant, wherein $K = \frac{16\pi\gamma^3 v^2}{3k^3T^3}$, and then γ can be calculated by

$$\gamma = \left(\frac{3Kk^3T^3}{16\pi v^2}\right)^{1/3} \tag{9}$$

In this work, were HPC is used as the modifier of DL-met crystal morphology, the influence of HPC on crystal nucleation and growth was explored through experiments by the turbidity method and by single crystal growth, respectively, with the assistance of molecular dynamics (MD) simulation by calculating the intermolecular interaction energy, mean square displacement (MSD), and radial distribution function (RDF). Finally, a possible mechanism was proposed to discover the role of HPC in the modulation of crystal morphology from the perspective of nucleation and growth.

2. EXPERIMENTS AND METHODS

2.1. Materials. DL-met (99% purity) and hydroxypropyl cellulose (average molecular mass 100000, degree of substitution about 1.88) were purchased from Shanghai Aladdin Biochemical Technology Co.,

https://doi.org/10.1021/cbe.3c00024
Chem Bio Eng. 2024, 1, 704−714

Ltd. (Shanghai, China). All materials were employed without further purification.

2.2. Characterizations. Powder X-ray diffraction (PXRD, Ultimate IV, Rigaku, Akishima, Japan) was used to identify the crystal form of DL-met, using Cu Kα radiation (0.15406 nm) at a scan rate of 2°/min in the diffraction angle range 5−60° (2θ). The morphology of DL-met was observed by optical microscopy (HU 500M, HAYEAR, Shenzhen, China) and scanning electron microscopy (SEM, SU-3500, Hitachi, Tokyo, Japan). The surface morphology and roughness were observed by atomic force microscopy (AFM, Dimension XR, Bruker, American, Tapping Mode, Bellerica, MA).

2.3. Solubility Measurements. The solubility of DL-met in water and HPC solution was determined by a laser dynamic method in the temperature range of 293.15−333.15 K with HPC concentrations of 50, 500, and 1000 ppm, respectively. After a certain amount of DL-met was weighed into the crystallization kettle (500 mL, Julabo, Seelbach, Germany), the temperature of the solution was controlled by a heating−cooling circulator (CF31, Julabo, Seelbach, Germany) and the transparency of the solution was monitored by a laser emitter (PA3223, Thorlabs, Bangkok, Thailand) and a laser power controller (HNL020L, Thorlabs, Bangkok, Thailand). The solution was clarified when the laser intensity through the solution reached the maximum value, which meant that the solute was completely dissolved. Continuing to add a small mass of DL-met until the laser intensity declined abruptly failed to return to the maximum, which means that the solution is saturated at this point. The above operations were repeated three times for each set of data to eliminate chance errors. The molar fraction solubility (x) of DL-met was calculated by the following equation

$$x = \frac{m_1/M_1}{(m_1/M_1) + (m_2/M_2) + (m_3/M_3)} \tag{10}$$

where m_1, m_2, and m_3 refer to the mass of DL-met, water, and HPC, respectively. Similarly, M_1, M_2, and M_3 denote the relative molecular masses of DL-met, water, and HPC, respectively.

2.4. Crystallization Experiments. Well-shaped DL-met crystals were prepared by slow evaporation of solvent from its solution with and without HPC. DL-met (3.0 g) was dissolved in distilled water (100 g) at 298.15 K, and then 2 mL of the solution was quickly filtered with a filter of 0.45 μm pore size and injected into a glass Petri dish covered by parafilm with 15 small uniform holes. After the crystal grew for a certain period, the crystal morphology was observed by optical microscopy and scanning electron microscopy.

2.5. Crystal Nucleation Experiments. The nucleation induction time of DL-met was determined by the turbidity method.[23,31,32] Detailed operations are as follows: A certain supersaturation of the DL-met solution was added to the crystallization kettle. HPC was then put into the solution and dissolved to reach concentrations of 0, 25, 50, and 100 ppm. Subsequently, the laser emitter was turned on, and the heating−cooling circulator was set to 308.15 K to completely dissolve the solid particles, at which time the laser intensity reached its maximum. Then the temperature is rapidly lowered to 298.15 K from which the time recording starts and stops when the laser intensity drops sharply. The time gap between the two recordings is the crystal nucleation induction time. The above operations were repeated by changing the solution supersaturation and the additive concentration, and each experiment was repeated at least three times to ensure the accuracy of the results. Eventually, the nucleation rate was calculated by eq 6.

2.6. Crystal Growth Experiments. Well-formed and collectible DL-met crystal seeds were obtained by slow evaporation solvent from its solution with 25 ppm of HPC at 298.15 K. Based on the solubility data, supersaturated solutions of DL-met at 298.15 K were prepared with HPC concentrations of 0, 25, 50, and 100 ppm. The solution (2 mL) was then quickly filtered with a 0.45 μm syringe filter to remove impurities and then transferred to a 5 mL glass dish containing single crystal seed. To avoid burst nucleation, glass dishes were sealed and placed in a constant temperature incubator (303-0B, Mingtu, Xuchang, China) at a controlled temperature of 298.15 K. The crystal morphology and size were observed under the optical microscope at regular intervals, and the relative growth lengths δd in the axial and radial directions of the crystal are measured as shown in eq 11. The relative growth length per unit time is the average growth rate of the crystal.

$$\delta d = d_2 - d_1 \tag{11}$$

where d_1 and d_2 are the initial lengths and the lengths after a period of growth of the crystal seeds, respectively.

2.7. Theoretical Computation. *2.7.1. Crystal Structures and Force Fields.* The initial cell structure[33] of the β form DL-met was obtained from the Cambridge Crystallographic Data Center database (CCDC no. 1063335). The crystallographic data and cell structures are shown in Table 1 and Figure 1(b), respectively. The cell contains eight DL-met molecules with a $C2/c$ space group and belongs to the monoclinic crystal system. The Dreiding force field (DFF) is used for geometry optimization and molecular dynamics calculations (Materials Studio (MS) 7.0, Accelrys Inc.) as it allows accurate optimization of lattice parameters and stable calculation of the DL-met crystal surface. The lattice parameters optimized by different force fields and the experimental data are listed in Table S1. The van der Waals force was calculated by the atom-based summation method with a cutoff radius of 12.5 Å; the Ewald method was chosen to compute the electrostatic interactions.

Table 1. Crystallographic Data of DL-met

crystal form	α	β (320 K)	β (105 K)	γ
space group	$I2/c$	$C2/c$	$P2_1/c$	$C2/c$
a (A)	16.74	31.77	33.13	31.76
b (A)	4.70	4.70	4.70	4.70
c (A)	9.89	9.89	9.88	9.90
β (deg)	102.3	91.22	106.3	90.98
crystal system	monoclinic	monoclinic	monoclinic	monoclinic
Z	4	8	8	8

2.7.2. Molecular Modeling and Dynamics Simulations. The morphological crystal surfaces of DL-met are mainly (200), (111), and (20$\bar{2}$) surfaces, as shown in Figure 1(c). Among them, the (111) and (20$\bar{2}$) crystal surfaces represent the axial and radial growth directions, respectively. Therefore, the subsequent calculations mainly focus on the (111) and (20$\bar{2}$) facets. The simulation steps are as follows: First, the (111) and (20$\bar{2}$) surfaces were cut with a thickness of 3 × d_{hkl} and expanded into 6 × 8 and 13 × 3 supercells, respectively. Then a vacuum layer with a thickness of 100 Å was set above the crystal surface as layer one to eliminate the boundary effect. A solution box as layer two containing 2000 water molecules and 20 DL-met molecules was constructed using the Amorphous Cell module, which was employed to simulate a solution model without additives. The same model with an additional HPC molecule including 5 monomers was constructed to evaluate the solution model in the presence of HPC. The above layer one and layer two were combined to construct the solution−crystal surface model, as shown in Figure S1, with a distance of 3 Å in the middle, and a vacuum layer of 400 Å thickness was constructed above layer two. After geometry optimization of the solution−crystal surface composite layer structure, MD simulation was performed at 298.15 K with a time step of 1 fs for 2 ns using an NVT ensemble. The temperature control function was chosen by the Andersen thermostat. Based on the analysis of stable structures from dynamics with DFF, the geometry of the HPC bonded to the crystal layer was obtained, and the solvent and solutes were removed for higher precision calculation. Therefore, the single-point energy was calculated using the GFN2-xTB[34] method, a semi-empirical density functional theory (DFT) from the xTB package[35] (Version 6.6.0), with the ALPB implicit solvent model[36] employed to correct the solvation effects. Then the adsorption energy E_{ads} between the additive molecule and the crystal layer was calculated as follows

https://doi.org/10.1021/cbe.3c00024
Chem Bio Eng. 2024, 1, 704−714

$$E_{ads} = E_{cry+HPC} - E_{cry} - E_{HPC} \quad (12)$$

where $E_{cry+HPC}$, E_{cry}, and E_{HPC} are single-point energies of the composite structure of the HPC bonded to the crystal layer, the crystal layer, and the HPC, respectively.

2.7.3. Radial Distribution Function (RDF) and Mean Square Displacement MSD. The structures within the equilibrium of 1 ns from MD simulations were taken to further analyze the radial distribution functions to describe the interaction of solute, solvent, and additive molecules with the crystal surface. Radial distribution functions[37,38] are defined as the ratio $g(r)$ of the probability density $\rho(r)$ of a particle distributed around a given particle in a certain distance to the probability of a random distribution ρ:

$$g(r) = \frac{\rho(r)}{\rho} \quad (13)$$

Thus, the RDF is a characterization of the probability that other particles are distributed around a given particle.[39,40] In addition, we focused on the attachment process of the clusters to better describe the effect of additives on the nucleation behavior. Based on the Szilard−Farkas continuous attachment and detachment model, MSD was used to observe the mobility of solute molecules in solution and additive molecules at crystal surfaces.[28] The two solution boxes in section 2.7.2 were annealed for kinetic calculations for pre-equilibration before calculating the molecular dynamics, and the *NVT* ensemble was used to perform MD calculations at 298.15 K with a time step of 1 fs for 2 ns. The 1000 trajectories of dynamic equilibrium were taken for the MSD calculation. Based on the Einstein diffusion equation, MSD can be used to evaluate the diffusion coefficient of a particle undergoing random Brownian motion in three-dimensional space. The equation is defined as follows,[25,41]

$$D = \frac{1}{6N_\alpha} \lim_{t\to\infty} \frac{d}{dt} \sum_{u=1}^{N_\alpha} \langle [r_i(t) - r_i(0)]^2 \rangle \quad (14)$$

where $N\alpha$ is the number of diffusing atoms in the system, r_i represents the position vector of atom α, and "$r_i(t) - r_i(0)$" refers to the vector distance between the initial and time t positions of the molecule. In this system, the derivative of the sum of the squares of the vector distances of N atoms concerning time is proportional to the diffusion coefficient.

3. RESULTS AND DISCUSSION

3.1. Influence of HPC on Crystal Properties. Solubility is a basic parameter that guides the solution crystallization process. The solubility data of DL-met at 293.15−313.15 K with additive concentrations of 50, 500, and 1000 ppm are shown in Figure 2. It can be seen that the solubility of DL-met gradually increases with the increase of solution temperature and declines as the additive concentration increases. It did not change notably in the presence of a low concentration of HPC, which might be due to the large number of hydroxyl groups on HPC molecules that can easily form hydrogen bonds with solvent molecules. As shown in Figure 3, DL-met crystal morphology appears as a long rod in water solution, while it displays a blocky hexahedral shape in the presence of low concentration HPC. This illustrates that HPC significantly affects the crystallization process of DL-met and inhibits the crystal growth in the axial direction, which leads to a remarkable decrease in the crystal aspect ratio. Furthermore, as shown in Figure 4, PXRD patterns of DL-met crystals with and without HPC were similar, which means that HPC did not penetrate into the crystal lattice and DL-met remains in its β form.

3.2. Influence of HPC on Nucleation Kinetics. The DL-met nucleation induction time with and without HPC is displayed in Figure 5. It could be seen that the nucleation induction time became shorter with the increase in supersaturation, which shows that the increase in supersaturation is beneficial to the formation of nuclei. Moreover, the nucleation

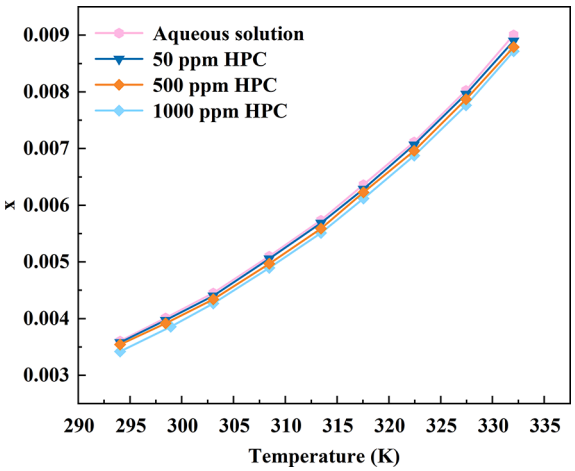

Figure 2. Solubility data of DL-met in water and solutions with different HPC concentrations.

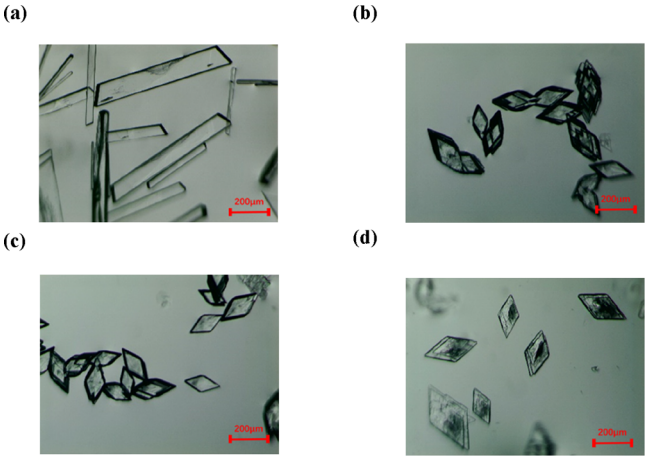

Figure 3. Crystal morphology of DL-met in water and solutions with different HPC concentrations: (a) water, (b) 25 ppm of HPC, (c) 50 ppm of HPC, and (d) 100 ppm of HPC.

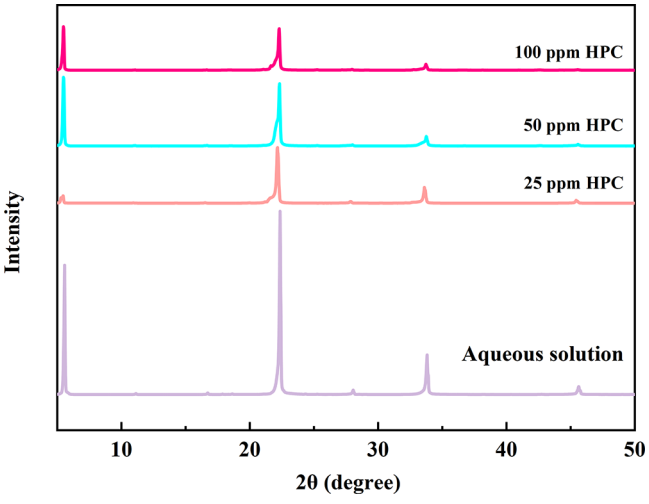

Figure 4. PXRD patterns of DL-met crystals obtained from water and solutions with different HPC concentrations.

https://doi.org/10.1021/cbe.3c00024
Chem Bio Eng. 2024, 1, 704−714

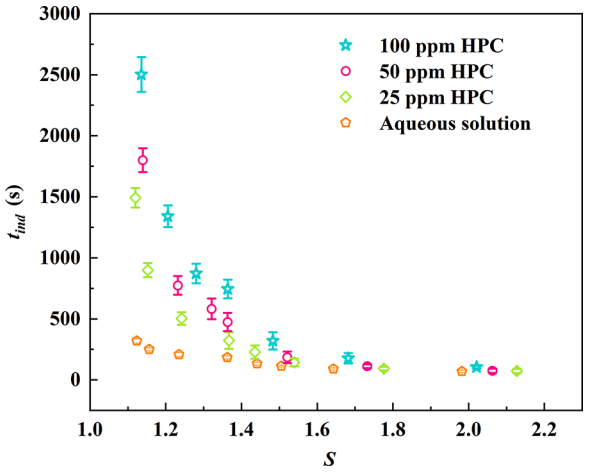

Figure 5. Nucleation induction times of DL-met with and without HPC.

induction time is prolonged gradually as the HPC concentration increases, which implies that HPC inhibits nucleation and can be used as a nucleation inhibitor for the DL-met crystallization process. Besides, the results of DL-met nucleation induction time fitted by CNT with and without HPC are shown in Figure 6. High regression coefficient values (R^2 > 0.97) suggest a well-linear fit. Two straight lines with different slopes were fitted according to the experimental results, and the turning point is the separation between heterogeneous and homogeneous nucleations. Heterogeneous nucleation dominates at lower supersaturation, while the nucleation process is controlled by homogeneous nucleation at higher supersaturation. Meanwhile, the linear relationship between $\ln t_{ind}$ and $1/\ln^2 S$ is still maintained in the presence of HPC, demonstrating that CNT can also reasonably describe the nucleation process of DL-met in the presence of HPC. The fitting results of the nucleation kinetic parameters are shown in Table 2. It could be seen that the interfacial energy γ increases with the increase of HPC concentration at a constant saturation temperature. γ reflects the level of difficulty of crystal nucleation. The nucleation is driven by the chemical potential difference, which is mainly determined by the Gibbs free energy, and an increase in γ leads to an increase in Gibbs free energy, thereby making the nucleation process more difficult. In addition, the relationship between nucleation rate and supersaturation and HPC concentration is shown in Figure 7. The introduction of HPC not only causes a competitive

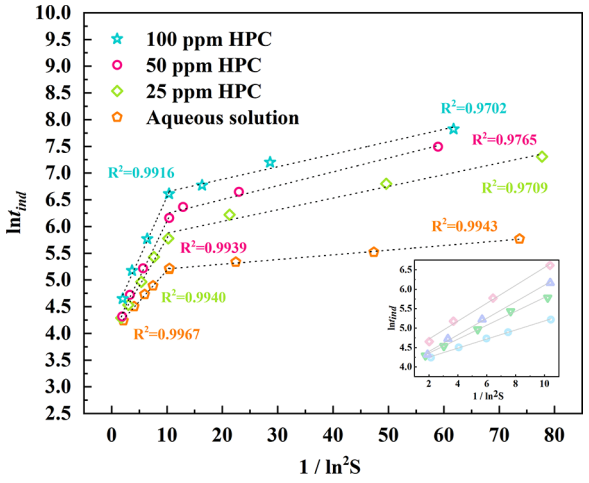

Figure 6. Fitting results of the CNT equation with and without HPC.

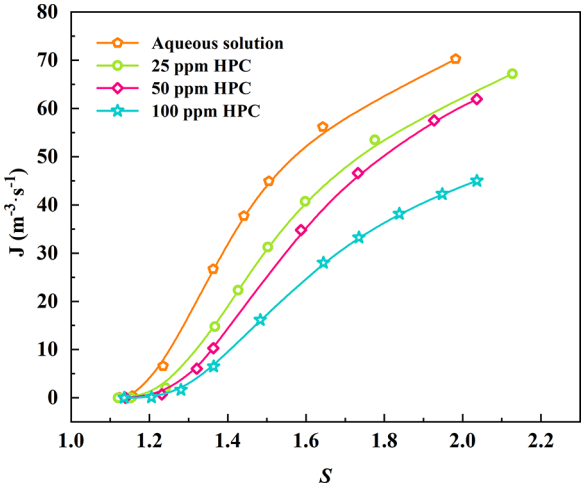

Figure 7. Nucleation rates at different HPC concentrations.

effect with DL-met molecules, which reduces the frequency of solute molecule adsorption, but also induces a rise in the nucleation barrier of DL-met and ultimately decreases the nucleation rate.

3.3. Influence of HPC on Growth Kinetics. Figure 8 demonstrates morphological change during the growth of DL-met crystal seeds with and without HPC. The crystals grow rapidly in the axial direction within 24 h in water solution, while the radial growth is not obvious. The growth rate of the crystals in the axial direction is much faster than that in the radial direction, and the crystals grow from the initial hexagonal block-like to the shuttle-like. In contrast, the crystal growth is slow within 24 h and accelerates in the range from 24 to 48 h in the presence of HPC; the crystal gradually grows into a hexagonal block with a small aspect ratio, and the crystal axial growth rate is slower than that of the radial direction. With the increase of HPC concentration, the axial growth of crystals is not significant, while radial growth is accelerated. It suggests that HPC inhibits crystal growth in the axial direction. To quantitatively characterize the effect of HPC on the crystal growth rate, the relative crystal growth lengths axially and radially at different hours were measured respectively as shown

Table 2. Thermodynamic and Kinetic Parameters of Nucleation Based on the CNT Fitting

Concentration (ppm)	B	K	R^2	γ (mJ·m^{-2})
0	4.0161 ± 0.0225	0.1165 ± 0.0034	0.9967	0.2468 ± 0.0239
25	3.9957 ± 0.0443	0.1788 ± 0.0070	0.9940	0.2847 ± 0.0368
50	3.9699 ± 0.0602	0.2131 ± 0.0097	0.9939	0.3018 ± 0.0457
100	4.2557 ± 0.0790	0.2230 ± 0.0122	0.9916	0.3095 ± 0.0549

https://doi.org/10.1021/cbe.3c00024
Chem Bio Eng. 2024, 1, 704−714

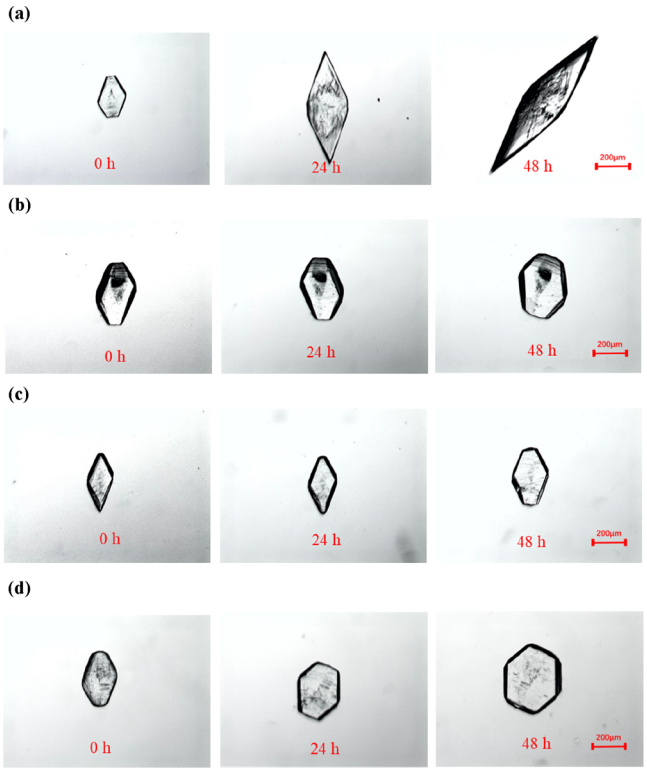

Figure 8. Growth of DL-met crystal seeds photographed by optical microscopy: (a) water, (b) 25 ppm of HPC, (c) 50 ppm of HPC, and (d) 100 ppm of HPC.

in Figure 9. The average axial and radial growth rates of the crystals over 48 h are listed in Table 3 and Figure 10. The axial

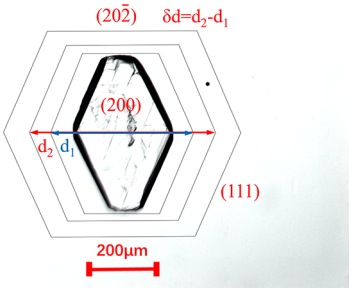

Figure 9. Relative growth lengths of DL-met crystal seeds.

growth rate is much faster than the radial growthin water solution, which is also consistent with the fact that the crystal habit of DL-met in water usually appears as long rod-like or needle-like. In the presence of HPC, the axial growth rate of crystals decreases significantly, meaning that the adsorption effect of HPC in the axial direction is stronger and crystal

Table 3. Growth Rates (μm·h^{-1}) of Crystals under the Effect of Different HPC Concentrations

Concentration (ppm)	Axial direction	Radical direction
0	29.648	2.496
25	1.407	0.959
50	2.226	1.357
100	2.558	2.438

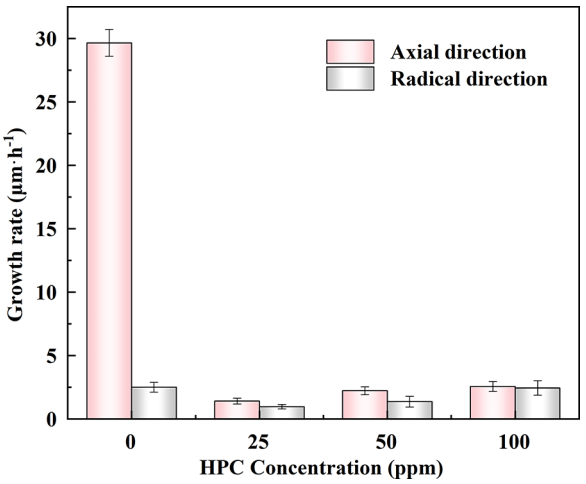

Figure 10. Growth rates of crystals at different HPC concentrations.

growth requires overcoming certain disassociation energy barriers, which leads to slower axial growth. With the increase in HPC concentration, the growth rates in both the axial and radial directions increase. These experimental results imply that HPC causes the solubility decrease of DL-met; i.e., increasing HPC concentration will raise the supersaturation of the solution with the same solute mass. And supersaturation is the main driving force for crystal growth; thereby, the growth rate will increase.

3.4. Crystal Growth Mechanism. The crystal surface morphology was analyzed by SEM and AFM to explore the crystal growth mechanism. As shown in Figure 11(a), the crystal surface (200) with the largest area share forms multiple uniform steps in the absence of HPC, which is consistent with the layered growth mode. Typically, the 2D nucleation growth mechanism considers that the individual growth unit adsorbs onto the surface and clusters together to form several 2D nuclei and leads to the appearance of twists and steps, which grow and spread until they reach the boundary.[42] It can be seen from Figure 11(b) that many uneven steps and kinks appear on the surface of (200) in the presence of HPC, probably due to the adsorption and steric hindrance effect of HPC on the crystal surface, which gives a large difference in the growth rate of steps and leads to the formation of uneven steps. Figure 12(a) illustrates that the (200) crystal surface grows layer by layer in the absence of HPC, where the "2D nucleation growth" mechanism occurs. As shown in Figure 12(b), the (200) surface is rougher in the presence of HPC, and steps and 2D islands appear on the crystal surface. Above all, there are many steps and almost no 2D islands on the crystal surface without HPC, which indicates that layer spread is more likely to occur on the crystal surface than nucleation, and it belongs to "mononuclear growth" in "2D nucleation growth" mechanism. In the presence of HPC, there are 2D islands on the crystal surface, and the spread of step and twist is not significant, which means that nucleation is more likely to occur on the crystal surface than layer spread, which can be explained with the "polynuclear growth" mechanism.

3.5. Analysis of Molecular Simulations. Two solvent systems were constructed, and MD calculations were performed to evaluate the diffusion of DL-met and HPC in solution by using MSD, and the results are shown in Figure 13. MSD was graphed against the simulation time, and the relationship is approximately linear, as shown in Figure 13(a),

https://doi.org/10.1021/cbe.3c00024
Chem Bio Eng. 2024, 1, 704−714

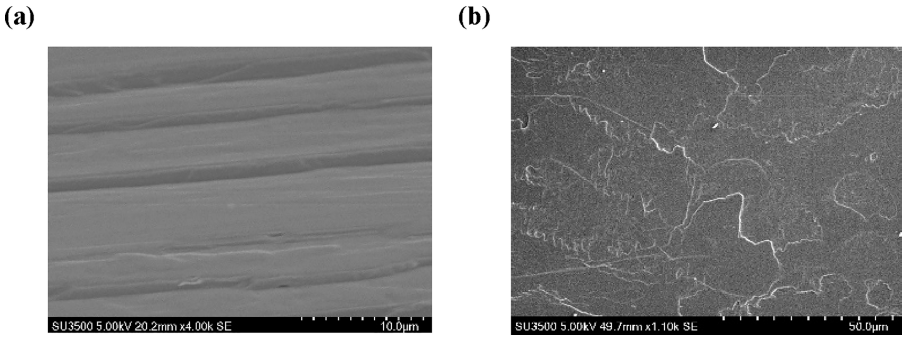

Figure 11. SEM images of the surface morphology of the (200) crystal surface: (a) without HPC and (b) with 50 ppm of HPC.

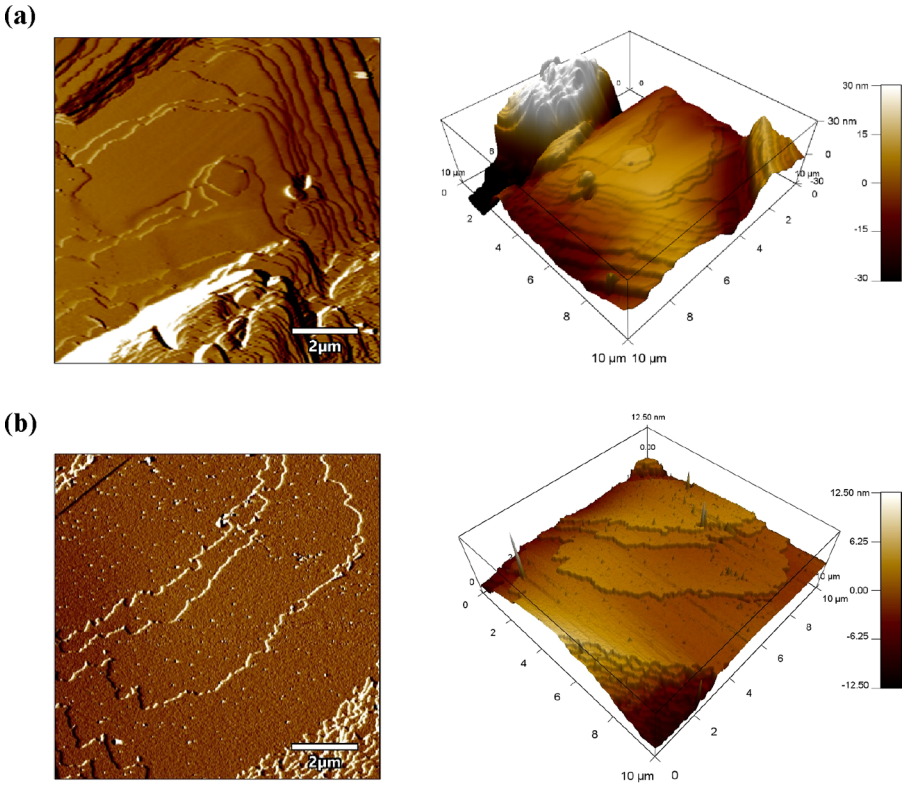

Figure 12. AFM images of the surface morphology of the (200) crystal surface: (a) without HPC and (b) with 50 ppm of HPC.

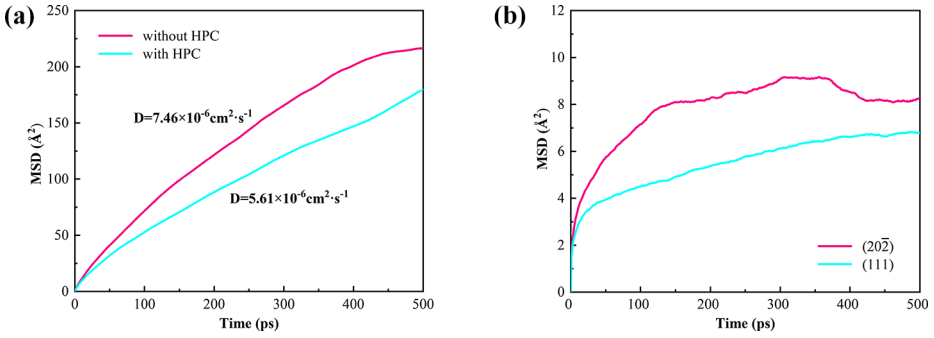

Figure 13. (a) MSD of DL-met. (b) MSD of HPC on (20$\bar{2}$) and (111) crystal surfaces.

suggesting that a normal diffusion state was reached. The diffusion coefficient was thus calculated as 7.46×10^{-6} cm^2/s in pure aqueous solution and 25% lower in solution with HPC. That is, HPC significantly reduces solute diffusion since its strong steric hindrance prevents DL-met molecules from interconnecting, thus reducing the attachment frequency among solute molecules to further form clusters. Similarly, it is difficult for the clusters to aggregate and grow into larger nuclei, which further explains the role of HPC in nucleation inhibiting. Figure 13(b) shows the MSD of HPC on (20$\bar{2}$) and (111) facets. The higher MSD of the (20$\bar{2}$) surface indicates that the mobility of HPC molecules on the (20$\bar{2}$) surface is

https://doi.org/10.1021/cbe.3c00024
Chem Bio Eng. 2024, 1, 704−714

much faster than the (111) facet and may cause the stronger interaction between HPC and the (111) surface. To further illustrate the competitive adsorption among HPC, the solvent and solutes, the RDFs for HPC−surface, solvent−surface, and solute−surface on both crystal surfaces were calculated. The results shown in Figure S2 reveal that HPC has a stronger influence on the (111) crystal surface than (20$\bar{2}$). Based on the results of MSD and RDFs, most likely, HPC interacts more strongly with the (111) surface and prevents the adsorption of solute molecules on the (111) crystal surface, which contributes to the decline of growth rates in the axial direction.

3.6. Interaction Analysis. The adsorption energy is direct evidence of the interaction strength between HPC and different crystal surfaces, which was calculated and is listed in Table 4. The adsorption energy between HPC and (111) crystal surface is much more negative than that of (20$\bar{2}$), meaning that the adsorption of HPC on the (111) crystal surface is much stronger than that of the (20$\bar{2}$) surface.

Table 4. Adsorption Energy of HPC and Crystal Surfaces

Crystal face	$E_{cry+HPC}$ (Hartree)	E_{cry} (Hartree)	E_{HPC} (Hartree)	E_{ads} (kcal·mol^{-1})
(111)	−2487.02947	−1828.71181	−658.21229	−66.12
(20$\bar{2}$)	−2547.99499	−1889.65113	−658.26874	−47.14

To better understand the intermolecular interactions between HPC and crystal surfaces intuitively, noncovalent interaction (NCI)[43] analysis was performed by Multiwfn[44] and VMD,[45] using the wave function generated by xTB. A typical local NCI isosurface is shown in Figure 14. Specifically, the carboxylate of DL-met acts as an acceptor to form H-bonds with the O−H and C−H of HPC. Meanwhile, the ammonium of DL-met acts as a donor to form H-bonds with the oxygen atoms of HPC. The full-scale NCI isosurface of the (111) and (20$\bar{2}$) crystal surfaces with HPC can be seen in Figure S4. The former demonstrates a larger and bluer isosurface, which indicates stronger interactions compared to the latter, particularly hydrogen bonding. Considering that H-bonds are significantly stronger than general van der Waals interactions, it can be concluded that the difference in adsorption energy is mainly due to H-bonds.

From the NCI analysis, it is clear that the H-bonds between the additive and crystal faces play a predominant role in the noncovalent interaction. Then RDFs of O−H$_{HPC}$···O$_{DL\text{-met}}$, C−H$_{HPC}$···O$_{DL\text{-met}}$, and N−H$_{DL\text{-met}}$···O$_{HPC}$ between HPC and crystal surfaces were further calculated, as shown in Figure 15, which is more statistically significant. Specifically,

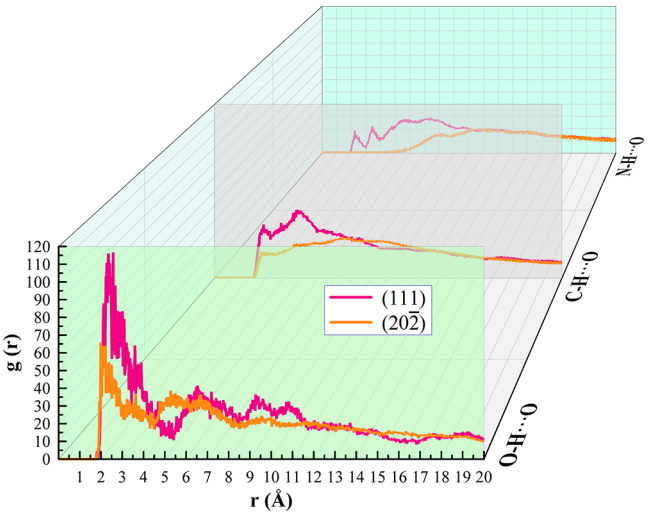

Figure 15. RDFs of different hydrogen bond patterns between the HPC and DL-met crystal surfaces.

$g(r)_{C-H\cdots O}$, $g(r)_{O-H\cdots O}$, and $g(r)_{N-H\cdots O}$ are much stronger at the (111) crystal surface than at (20$\bar{2}$), and the intensities of O−H···O and N−H···O are stronger than the atypical hydrogen bond C−H···O.[46] That is, the intensity of H-bonds between the additive and the (111) crystal surface is stronger than that with the (20$\bar{2}$) surface. The underlying reasons for the significant difference in H-bonds between HPC and the two crystal faces were further analyzed and found to be strongly correlated with the structure. As shown in Figure 1(d),(e), the carboxylate is nearly perpendicular to the growth direction of the crystal surface, and both oxygens can act as

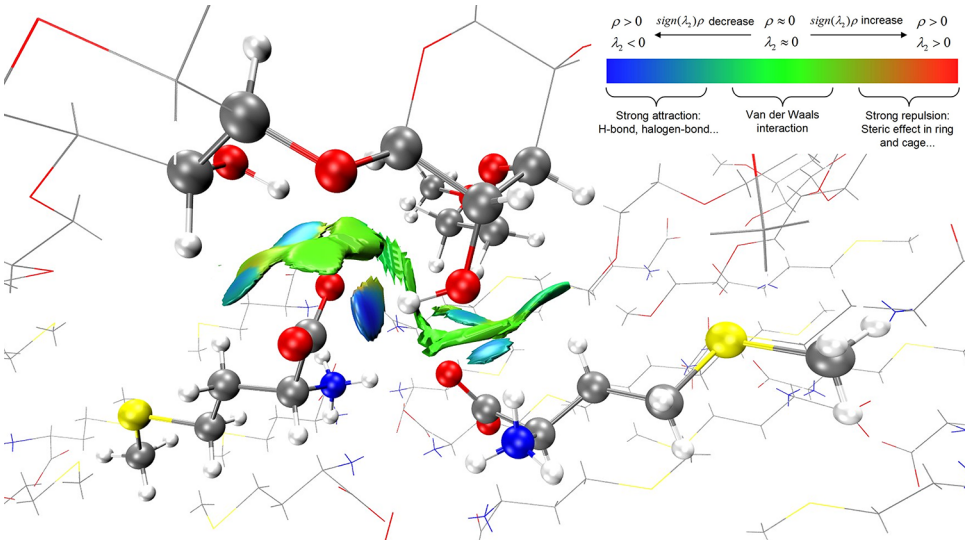

Figure 14. NCI gradient isosurface (s = 0.5 au) for HPC and the (111) crystal surface.

https://doi.org/10.1021/cbe.3c00024
Chem Bio Eng. 2024, 1, 704−714

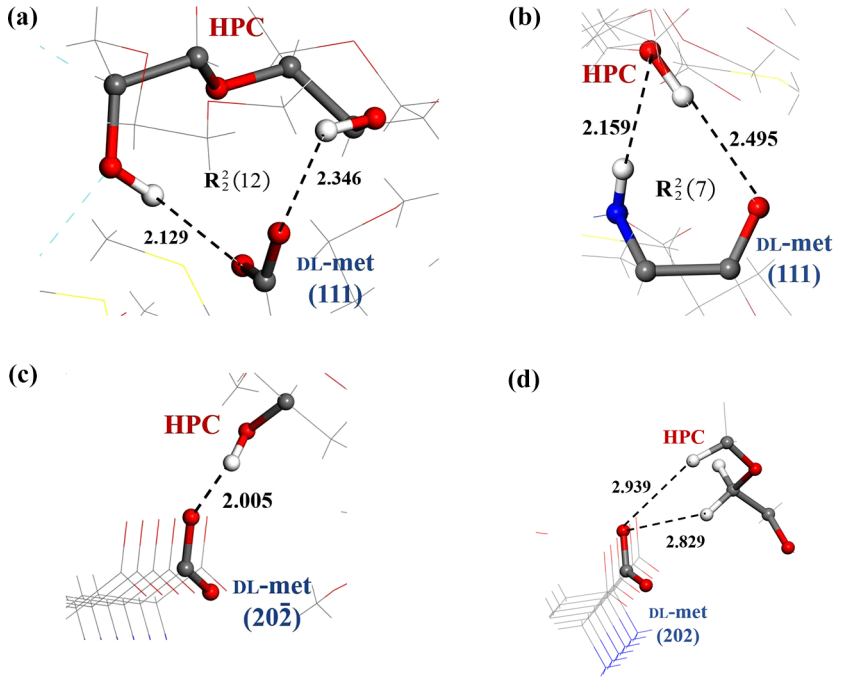

Figure 16. Hydrogen bond patterns between HPC and DL-met crystal surfaces: (a, b) (111) crystal surface; (c, d) (20$\bar{2}$) crystal surface.

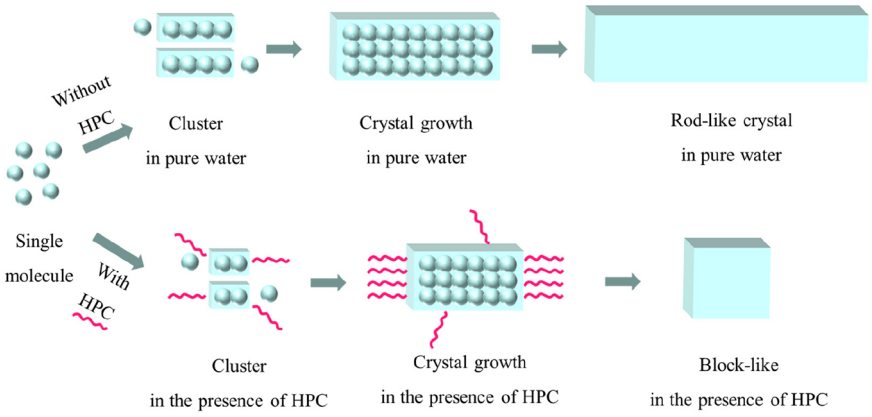

Figure 17. Schematic diagram of the DL-met morphology regulation mechanism by HPC.

hydrogen bonding acceptors susceptible to interact with HPC on the (111) crystal surface. Meanwhile, the ammonium alternates with the carboxylate and acts as a donor; i.e., the hydrogen bond donors and acceptors are concentrated and cross-arranged on the (111) crystal face. However, the carboxylate has only one oxygen atom facing toward the (20$\bar{2}$) surface above, and the other oxygen atom is diagonally downward along the face, which is not easy to interact with the hydrogen atoms of HPC. In addition, the ammonia is arranged above the second layer but below the first layer, which makes it difficult to interact with the oxygen atoms of HPC. More specially, since the (111) crystal surface can provide more H-bond donors and acceptors with concentrated distribution for HPC, some H-bond rings were found between the (111) crystal surface and HPC. Figure 16 panels (a) and (b) show two typical H-bond rings between HPC and the (111) face, named as $R_2^2(8)$ and $R_2^2(12)$ based on the literature.[47] These H-bond rings further enhance the bonding between the two molecular fragments, thereby making it difficult to dissociate, while a similar phenomenon was not observed on the (20$\bar{2}$) crystal surface. The hydrogen bonding patterns formed between the (20$\bar{2}$) surface and HPC primarily consist of simple H-bonds and several bifurcated H-bonds, as illustrated in Figure 16(c),(d). It is convinced that the (20$\bar{2}$) surface exhibits weaker binding with HPC compared to the (111) face. As a result, the strength of the H-bonds formed by the (111) crystal face with HPC is stronger than that of bonds with the (20$\bar{2}$) crystal face.

3.7. Modification Mechanism in the Presence of HPC.

The above theoretical analysis discloses a possible mechanism for the regulation of the DL-met crystal morphology by HPC, as shown in Figure 17. During the crystal nucleation process, the strong steric hindrance effect of HPC may prevent DL-met molecules from integrating with each other, which further impedes the formation of nuclei. Therefore, the nucleation rate decreases significantly in the presence of HPC. During the crystal growth process, HPC adsorbs to the (111) crystal face preferentially due to the stronger H-bond interaction in the axial direction. Furthermore, the solute molecules bind to the crystal growth sites much more strongly in the radial direction

https://doi.org/10.1021/cbe.3c00024
Chem Bio Eng. 2024, 1, 704−714

than in the axial direction, which causes much stronger inhibition of the axial growth rate by HPC than in the radial direction, resulting in a change in crystal morphology from rod-like to block-like.

4. CONCLUSIONS

The additive HPC transformed the DL-met crystal habit successfully, and its influence on the crystal nucleation and growth process was investigated from thermodynamic and kinetic perspectives, respectively. Theoretical calculations further unveil the mechanism of HPC regulation. On the experimental side, thermodynamic studies have shown that HPC reduces the solubility of DL-met to a certain extent. Additionally, HPC raised both the interfacial energy for nucleation, known as γ, and the Gibbs free energy, resulting in a decrease in the nucleation rate due to its strong steric hindrance. Kinetic studies revealed that HPC could inhibit the axial growth of crystals significantly; thereby, the low aspect ratio DL-met crystals were obtained. Interestingly, SEM and AFM discovered that HPC changes the growth mode of the (200) crystal surface from a mononuclear to a polynuclear growth mechanism.

Theoretical calculations were implemented to explain the underlying principles of HPC's role in DL-met crystallization. MSD calculations revealed that HPC inhibits the diffusion of solutes in solution, which reduces the aggregation of solutes and their clusters, making nucleation more difficult. RDFs indicated that HPC reduces the chance of solute contact with the (111) surface than the $(20\bar{2})$ surface to a greater extent, which ultimately resulted in a significant decrease in the axial growth rate and a morphological change of DL-met crystals from long rod-like to block-like. The stronger growth inhibition on the (111) surface can be attributed to the stronger binding between HPC and this surface, which was verified through a DFT adsorption energy calculation. Further interaction analysis suggested that hydrogen bonds could play a dominant role in the binding of HPC to the crystal surfaces and exhibit significant differences for different surface structures. This is the underlying mechanism through which the HPC regulates the crystal habits of DL-met.

This work may provide new insight into polymer additives in tuning crystallization behavior and deepen the understanding of how the hydrogen bond works based on different crystal structures.

■ ASSOCIATED CONTENT

Supporting Information

The Supporting Information is available free of charge at https://pubs.acs.org/doi/10.1021/cbe.3c00024.

Experimental and optimized crystal parameters of β (320 K) form DL-met by different force fields, schematic diagram of solution-crystal surface model, RDFs of (111) and $(20\bar{2})$ crystal surfaces with and without HPC, RDFs of solute−surface, solvent−surface, and HPC−surface on $(20\bar{2})$ and (111) crystal surfaces, and NCI gradient isosurfaces (s = 0.5 au) between HPC and crystal surfaces (PDF)

■ AUTHOR INFORMATION

Corresponding Author

Shenfeng Yuan − *College of Chemical and Biological Engineering, Zhejiang University, Hangzhou 310058, P.R. China; Zhejiang Key Laboratory of Advanced Chemical Engineering Manufacture Technology, Hangzhou 310058, P.R. China*; Email: ysf@zju.edu.cn

Authors

Hong Yin − *College of Chemical and Biological Engineering, Zhejiang University, Hangzhou 310058, P.R. China; Zhejiang Key Laboratory of Smart Biomaterials, Hangzhou 310058, P.R. China*; orcid.org/0000-0003-0742-3754

Sen Xia − *College of Chemical and Biological Engineering, Zhejiang University, Hangzhou 310058, P.R. China*; orcid.org/0009-0009-1316-2694

Zhirong Chen − *College of Chemical and Biological Engineering, Zhejiang University, Hangzhou 310058, P.R. China*

Complete contact information is available at: https://pubs.acs.org/10.1021/cbe.3c00024

Notes

The authors declare no competing financial interest.

■ ACKNOWLEDGMENTS

We are grateful for the computing resources of Sugon HPC, provided by the Computing Center of the College of Chemical and Biological Engineering, Zhejiang University. This research did not receive any specific grant from funding agencies in the public, commercial, or not-for-profit sectors.

■ REFERENCES

(1) Gao, Z.; Wang, X.; Tan, C.; Zhou, H.; Mai, K.; He, G. Effect of dietary methionine levels on growth performance, amino acid metabolism and intestinal homeostasis in turbot (Scophthalmus maximus L.). *Aquaculture* **2019**, *498*, 335−342.

(2) Chen, Z.; Zhou, R.; Yin, H.; Yuan, S. Determination and correlation of temperature andpHvalue dependent solubility of dl methionine. *AIChE J.* **2020**, *66* (8), e16270.

(3) Cheng, X.; Huang, X.; Hao, Y.; Wang, B.; Sun, C.; Shu, J.; Hao, H. Unveiling the Role of Additives in Modifying Crystallization Behaviors of 4-(Hydroxymethyl) Benzoic Acid. *Ind. Eng. Chem. Res.* **2022**, *61* (20), 7193−7203.

(4) de Albuquerque, I.; Mazzotti, M.; Ochsenbein, D. R.; Morari, M. Effect of needle-like crystal shape on measured particle size distributions. *AIChE J.* **2016**, *62* (9), 2974−2985.

(5) Hatcher, L. E.; Li, W.; Payne, P.; Benyahia, B.; Rielly, C. D.; Wilson, C. C. Tuning Morphology in Active Pharmaceutical Ingredients: Controlling the Crystal Habit of Lovastatin through Solvent Choice and Non-Size-Matched Polymer Additives. *Cryst. Growth Des.* **2020**, *20* (9), 5854−5862.

(6) Constance, E. N.; Mohammed, M.; Mojibola, A.; Egiefameh, M.; Daodu, O.; Clement, T.; Ogundolie, T.; Nwawulu, C.; Aslan, K. Effect of Additives on the Crystal Morphology of Amino Acids: A Theoretical and Experimental Study. *J. Phys. Chem. C* **2016**, *120* (27), 14749−14757.

(7) Goswami, H.; Seth, J. R. Influence of Surfactant on Crystallization Kinetics of Stearic Acid. *Ind. Eng. Chem. Res.* **2019**, *58* (18), 7661−7669.

(8) Yani, Y.; Chow, P. S.; Tan, R. B. Molecular simulation study of the effect of various additives on salbutamol sulfate crystal habit. *Mol. Pharmaceutics* **2011**, *8* (5), 1910−1918.

(9) Black, J. F. B.; Cruz-Cabeza, A. J.; Davey, R. J.; Willacy, R. D.; Yeoh, A. The Kinetic Story of Tailor-made Additives in Polymorphic Systems: New Data and Molecular Insights for p-Aminobenzoic Acid. *Cryst. Growth Des.* **2018**, *18* (12), 7518−7525.

(10) Chai, S.; Li, E.; Zhang, L.; Du, J.; Meng, Q. Crystallization solvent design based on a new quantitative prediction model of crystal morphology. *AIChE J.* **2022**, *68* (1), e17499.

(11) Li, Z.; Ma, Y.; Lin, J.; Gao, Z.; Wu, S.; Li, W.; Han, D.; Gong, J.; Wang, J. The polymorph and crystal habit control of dl-methionine assisted by ultrasound. *Journal of Crystal Growth* **2022**, *596*, 126818.
(12) Lovette, M. A.; Doherty, M. F. Needle-Shaped Crystals: Causality and Solvent Selection Guidance Based on Periodic Bond Chains. *Cryst. Growth Des.* **2013**, *13* (8), 3341−3352.
(13) Yin, H.; Ge, H.; Chen, Z.; Yuan, S. Growth behavior of β form DL-methionine crystal in the presence of inorganic acids and bases additives: A combination of experiments and molecular dynamics simulation study. *J. Cryst. Growth* **2022**, *587*, 126636.
(14) Li, Z.; Shi, P.; Yang, Y.; Sun, P.; Wang, Y.; Xu, S.; Gong, J. Tuning crystallization and stability of the metastable polymorph of DL-methionine by a structurally similar additive. *CrystEngComm* **2019**, *21* (24), 3731−3739.
(15) Zhang, Y.; Tian, X.; Zhang, Q.; Xie, H.; Wang, B.; Feng, Y. Hydrochar-embedded carboxymethyl cellulose-g-poly(acrylic acid) hydrogel as stable soil water retention and nutrient release agent for plant growth. *J.Bioresour.Bioprod.* **2022**, *7* (2), 116−127.
(16) Wang, J.; Euring, M.; Ostendorf, K.; Zhang, K. Biobased materials for food packaging. *J.Bioresour.Bioprod.* **2022**, *7* (1), 1−13.
(17) Atta, O. M.; Manan, S.; Ul-Islam, M.; Ahmed, A. A. Q.; Ullah, M. W.; Yang, G. Development and characterization of plant oil-incorporated carboxymethyl cellulose/bacterial cellulose/glycerol-based antimicrobial edible films for food packaging applications. *Adv. Compos. Hybrid Mater.* **2022**, *5* (2), 973−990.
(18) Wang, H.; Li, Z.; Yahyaoui, S.; Hanafy, H.; Seliem, M. K.; Bonilla-Petriciolet, A.; Luiz Dotto, G.; Sellaoui, L.; Li, Q. Effective adsorption of dyes on an activated carbon prepared from carboxymethyl cellulose: Experiments, characterization and advanced modelling. *Chem. Eng. J.* **2021**, *417*, 128116.
(19) Priyadarshi, R.; Kim, S.-M.; Rhim, J.-W. Carboxymethyl cellulose-based multifunctional film combined with zinc oxide nanoparticles and grape seed extract for the preservation of high-fat meat products. *Sustainable Mater. Technol.* **2021**, *29*, e00325.
(20) Kumar, A.; Rao, K. M.; Han, S. S. Mechanically viscoelastic nanoreinforced hybrid hydrogels composed of polyacrylamide, sodium carboxymethylcellulose, graphene oxide, and cellulose nanocrystals. *Carbohydr. Polym.* **2018**, *193*, 228−238.
(21) Chan, C. L. C.; Lei, I. M.; van de Kerkhof, G. T.; Parker, R. M.; Richards, K. D.; Evans, R. C.; Huang, Y. Y. S.; Vignolini, S. 3D Printing of Liquid Crystalline Hydroxypropyl Cellulose—toward Tunable and Sustainable Volumetric Photonic Structures. *Advanced Functional Materialsd* **2022**, *32* (15), 2108566.
(22) Barty King, C. H.; Chan, C. L. C.; Parker, R. M.; Bay, M. M.; Vadrucci, R.; De Volder, M.; Vignolini, S. Mechanochromic, Structurally Colored, and Edible Hydrogels Prepared from Hydroxypropyl Cellulose and Gelatin. *Adv. Mater.* **2021**, *33* (37), 2102112.
(23) Zhang, X.; Yang, Z.; Chai, J.; Xu, J.; Zhang, L.; Qian, G.; Zhou, X. Nucleation kinetics of lovastatin in different solvents from metastable zone widths. *Chem. Eng. Sci.* **2015**, *133* (8), 62−69.
(24) Diao, Y.; Helgeson, M. E.; Myerson, A. S.; Hatton, T. A.; Doyle, P. S.; Trout, B. L. Controlled nucleation from solution using polymer microgels. *J. Am. Chem. Soc.* **2011**, *133* (11), 3756−3759.
(25) Wu, H.; Wang, J.; Huang, X.; Zhai, L.; Hao, H. Enlarging crystal size of zoxamide by polymeric additives that modulate burst nucleation. *J. Mol. Liq.* **2022**, *357*, 119088.
(26) Wu, H.; Wang, J.; Liu, Q.; Zong, S.; Tian, B.; Huang, X.; Wang, T.; Yin, Q.; Hao, H. Influences and the Mechanism of Additives on Intensifying Nucleation and Growth of p-Methylacetanilide. *Cryst. Growth Des.* **2020**, *20* (2), 973−983.
(27) Li, H.; Chavez, A. D.; Li, H.; Li, H.; Dichtel, W. R.; Bredas, J. L. Nucleation and Growth of Covalent Organic Frameworks from Solution: The Example of COF-5. *J. Am. Chem. Soc.* **2017**, *139* (45), 16310−16318.
(28) Davey, R. J.; Schroeder, S. L.; ter Horst, J. H. Nucleation of organic crystals-a molecular perspective. *Angew. Chem. Int. Ed Engl* **2013**, *52* (8), 2166−2179.
(29) Li, J.; Deepak, F. L. In Situ Kinetic Observations on Crystal Nucleation and Growth. *Chem. Rev.* **2022**, *122* (23), 16911−16982.
(30) Kashchiev, D.; Verdoes, D.; Van Rosmalen, G. Induction time and metastability limit in new phase formation. *J. Cryst. Growth* **1991**, *110* (3), 373−380.
(31) Prisciandaro, M.; Olivieri, E.; Lancia, A.; Musmarra, D. PBTC as an Antiscalant for Gypsum Precipitation: Interfacial Tension and Activation Energy Estimation. *Ind. Eng. Chem. Res.* **2012**, *51* (39), 12844−12851.
(32) Jiang, S.; ter Horst, J. H. Crystal Nucleation Rates from Probability Distributions of Induction Times. *Cryst. Growth Des.* **2011**, *11* (1), 256−261.
(33) Gorbitz, C. H.; Paulsen, J. C.; Borgersen, J. Redetermined crystal structure of β- DL-methionine at 320 K. *Acta Crystallogr. E Crystallogr. Commun.* **2015**, *E71*, o398−o399.
(34) Bannwarth, C.; Ehlert, S.; Grimme, S. GFN2-xTB—An Accurate and Broadly Parametrized Self-Consistent Tight-Binding Quantum Chemical Method with Multipole Electrostatics and Density-Dependent Dispersion Contributions. *J. Chem. Theory and Comput.* **2019**, *15* (3), 1652−1671.
(35) Bannwarth, C.; Caldeweyher, E.; Ehlert, S.; Hansen, A.; Pracht, P.; Seibert, J.; Spicher, S.; Grimme, S. Extended tight binding quantum chemistry methods. *Wires Comput. Mol. Sci.* **2021**, *11* (2), e1493.
(36) Ehlert, S.; Stahn, M.; Spicher, S.; Grimme, S. Robust and Efficient Implicit Solvation Model for Fast Semiempirical Methods. *J. Chem. Theory Comput.* **2021**, *17* (7), 4250−4261.
(37) Schreiber, R. E.; Houben, L.; Wolf, S. G.; Leitus, G.; Lang, Z. L.; Carbo, J. J.; Poblet, J. M.; Neumann, R. Real-time molecular scale observation of crystal formation. *Nat. Chem.* **2017**, *9* (4), 369−373.
(38) Anwar, J.; Boateng, P. K. Computer Simulation of Crystallization from Solution. *J. Am. Chem. Soc.* **1998**, *120* (37), 9600−9604.
(39) Song, Y.; Cai, Z.; Li, Z.; Guan, G.; Jiang, Y. Preferential Orientation Effect of Polymers on Paracetamol Crystallization: Experiments and Modeling. *Cryst. Growth Des.* **2018**, *18* (9), 4987−4997.
(40) Yang, W.; Xu, D.; Diao, Y.; Zhao, J.; Jing, Z.; Guo, Y. Molecular dynamics simulations on K_2SO_4 nucleation in supercritical water. *J. Mol. Liq.* **2022**, *367*, 120565.
(41) Li, W.; Yang, J.; Du, S.; Macaringue, E.; Wang, Y.; Wu, S.; Gong, J. Preparation and Formation Mechanism of l-Valine Spherulites via Evaporation Crystallization. *Ind. Eng. Chem. Res.* **2021**, *60* (16), 6048−6058.
(42) Lovette, M. A.; Browning, A. R.; Griffin, D. W.; Sizemore, J. P.; Snyder, R. C.; Doherty, M. F. Crystal shape engineering. *Ind. Eng. Chem. Res.* **2008**, *47* (24), 9812−9833.
(43) Johnson, E. R.; Keinan, S.; Mori-Sánchez, P.; Contreras-García, J.; Cohen, A. J.; Yang, W. Revealing Noncovalent Interactions. *J. Am. Chem. Soc.* **2010**, *132* (18), 6498−6506.
(44) Lu, T.; Chen, F. Multiwfn: a multifunctional wavefunction analyzer. *J. Comput. Chem.* **2012**, *33* (5), 580−592.
(45) Humphrey, W.; Dalke, A.; Schulten, K. VMD: Visual molecular dynamics. *J. Mol. Graph.* **1996**, *14* (1), 33−38.
(46) Gu, Y.; Kar, T.; Scheiner, S. Fundamental Properties of the CH···O Interaction: Is It a True Hydrogen Bond? *J. Am. Chem. Soc.* **1999**, *121* (40), 9411−9422.
(47) Aakeroy, C. B.; Seddon, K. R. The Hydrogen Bond and Crystal Engineering. *Chem. Soc. Rev.* **1993**, *22* (6), 397−497.

https://doi.org/10.1021/cbe.3c00024
Chem Bio Eng. 2024, 1, 704−714